Title	Catalyst free growth of ZnO thin film nanostructures on Si substrate by thermal evaporation
Author(s)	M. Hassan, L. Jiaji, P. Lee and R. S. Rawat

Catalyst free growth of ZnO thin film nanostructures on Si substrate by thermal evaporation

M. Hassan[1,2*], L. Jiaji[2], P. Lee[2] and R. S. Rawat[2]

[1]Department of Physics, GC University, 54000 Lahore, Pakistan
[2]Natural Sciences and Science Education, National Institute of Education, Nanyang Technological University, 1 Nanyang Walk, Singapore 637616

Abstract

Zinc oxide (ZnO), a wide direct band gap (3.37 eV) II-VI semiconductor, is a fascinating technological material capable of exhibiting both semiconducting and piezoelectric characteristics and distinguished performance in photonics and optoelectronics. We report the synthesis of ZnO thin films composed of randomly oriented, 1-dimensional (1-D) and multipod (tripod and tetrapod)-like nanostructures of varying diameters by thermal evaporation technique. ZnO films of 150 nm thickness were grown for various deposition rates on room temperature Si and pyrex substrates by evaporating catalyst-free ZnO powder. X-ray diffraction (XRD) analysis of the films confirmed polycrystalline nature of wurtzite ZnO nanostructures with lattice constants of $a = b = 3.24$ Å and $c = 5.2$ Å. Field emission scanning electron microscopy (FESEM) and high resolution transmission electron microscopy (HRTEM) analysis revealed a strong influence of film deposition rate on the morphology of nanostructures. For a typical deposition rate of 0.04 nm/sec, aligned 1-D vertically oriented ZnO nanowires of 50 - 60 nm diameter having lattice spacing of 5.2 Å with [0001] facet were grown. Energy dispersive x-ray spectroscopy (EDS) has confirmed spatially uniform high quality ZnO nanostructures growth. Micro-Raman spectra of the films confirmed appearance of characteristic longitudinal optical (LO) and transverse optical (TO) modes of wurtzite ZnO dependent on the deposition rate. The nanostructure formation is via a multiphase polytypic growth

process depending on precursor growth to deposition ratio, thus promoting a particular growth facet by the crystal growth kinetics under those conditions.

KEYWORDS: Deposition rate, HRTEM/SAED, nanostructures, Raman spectroscopy, thermal evaporation.

***Corresponding author:** hassanjh@gmail.com (M. Hassan)

1. Introduction

The prospect of multifunctional materials such as piezoelectrics, magnetostrictive materials, shape memory alloys and piezomagnetic materials as thin films has provided an impetus to grow such smart materials with tailored functionalities including gas sensitivity, piezoelectricity, and photoconductivity [1]. Nanostructures of zinc oxide (ZnO) are receiving enormous attention owing to their potential applications in microelectromechanical and nanoelectromechanical systems (MEMS and NEMS) as building blocks for nanodevices [2, 3]. Eventually, after the first discovery of ZnO nanobelts [4], considerable efforts have been devoted to synthesize and characterize ZnO nanostructures with diverse and abundant configurations including nanosprings [5], nanorings [6], nanopropellers, nanohelices [7], nanocombs [8], aligned nanowire arrays [9], nanoaeroplanes and tetrapod-like networks [8, 10]. Quite recently, technological advancement in ZnO heterostructures for the possibility of device functionalities to various kinds of applications has been reviewed [11, 12]. Among the known 1-dimensional (1-D) nanomaterials, ZnO has the advantages of offering both semiconducting and piezoelectric properties that can form the basis for electromechanically coupled sensors and transducers [13]. Moreover, ZnO is relatively biosafe and biocompatible that can be employed for biomedical applications with little toxicity [14] as well as hydrophobic and antimicrobial nanoelement additive in cement composites [15]. 1-D ZnO nanowires have been used as building blocks for electric nanogenerators [3, 16- 19]. Such nanogenerators could be the basis for new self-powering nanotechnology as miniaturized integrated nanosystems for optoelectronics [20], biosensors [21] and other applications.

Nanoscale tetrapods are promising candidates for active components in diverse technological fields due to their remarkable properties [22, 23]. Tetrapods are superior in providing electron extraction to 1-D nanorod structures or bulk materials as interconnections and functional components in photovoltaic devices [22, 24]. In recent years, owing to the requirement of device design and controlled synthesis, the lattice structure and formation mechanism of ZnO nano-tetrapods have received significant attention. Structural non-homogeneity within the arrays of ZnO nanowires were studied to reveal the gradient of the nanowires and the parameters affecting the growth mechanisms [25]. Although numerous studies have demonstrated novel nanodevices and applications based on nanostructures particularly aligned ZnO nanowires [9, 10, 16-19, 26, 27], still much work is needed to address their growth parameters and thermal stability conditions.

ZnO nanostructures can be grown by chemical vapor deposition (CVD) [28], metal-organic vapor-phase epitaxy, metal-organic chemical vapor deposition (MOCVD) [29], thermal decomposition/physical vapor deposition (PVD) [3-6], hydrothermal process [30], microwave plasma [10], etc. Regarding the yield, thermal evaporation is a simpler and cost-effective technique with mass production of ZnO nanowires, nanoribbons, and needle-like rods [31]. The synthesis of high quality ZnO nanostructures usually requires high temperatures [5, 6], catalysts or additives [9]. For possible integration with general substrates, the ZnO growth has to be at low temperature. Also, the nanowires have to be grown following a designed pattern, with a high degree of control on size, orientation, dimensionality, uniformity, and possibly shape. Moreover, the catalyst may need to be

eliminated for integration with silicon-based technology [32]. So, catalyst-free thermal evaporation processes were attempted to obtain variety of hetrostructures [4, 5, 33].

Existing literature on ZnO nanostructures mainly includes elevated temperature [4, 5] and activated reactive evaporation [8, 34] growth using thermal evaporation. Furthermore, ZnO nanostructured films are highly sensitive to UV light. Since the position of visible emission peak is found to vary with morphology of the nanostructured films, thus room temperature growth of ZnO hetrostructures using catalyst free substrate by simple thermal evaporation technique finds potential interest in UV photo-detection. To our best of knowledge, we first time report the synthesis of patterned ZnO hetrostructures including randomly oriented 1-D nanowires and multipods (tripods and tetrapods) selectively grown for different deposition rates on Si substrate at room temperature by thermal evaporation technique using catalyst free ZnO powder, and provide detailed investigations in context with their growth kinetics. We have performed systematic study on the synthesis of ZnO nanostructures, their structural, compositional and morphological characteristics as well as bond nature vis-a-vis deposition rate. The precursor growth vs deposition rate that is the major factor in controlling the geometry and size of the nanostructures is investigated and is presented in details.

2. Experimental

Thin films of ZnO nanostructures were grown on Si substrates by evaporating pellets of ZnO in HINDHIVAC-15F6 thermal evaporation system. Si samples of 10×10 mm^2 size were ultrasonically cleaned in acetone, ethanol and de-ionized water for 10 min each. High purity (99.999 %) ZnO powder was grinded by ball milling method and its calcination was carried out at 300 ^oC for 3 hours in ambient air. After calcination the

powder was pressed into the form of ZnO pellets and sintered at 500°C for 1 hour. Before the deposition process, a tungsten boat held between the electrodes is thermally cleaned by supplying a current of 100 A for 4 hours in the background air pressure of 10^{-6} mbar. The system is brought to room temperature by slow reduction of boat current in 5-6 hours. The ZnO pellets are then fed into the boat and vaporized when heated by a current of 140-190 A.

Before deposition, the system was evacuated down to a base pressure of 10^{-6} mbar, while 150 nm thick ZnO films were deposited for different deposition rates (0.01, 0.02, 0.04 & 0.06 nm/sec) in background air pressure of 5×10^{-6} mbar. The thin film lot for each deposition rate consists of 6-8 Si samples. A quartz crystal oscillator digital thickness monitor DTM-101, fed with density and acoustic impedance of ZnO, and tooling factor (%) for evaporant/monitor/substrate assembly, controls the deposition process by providing a direct display of the film thickness and the deposition rate. To achieve uniform deposition, the sample holding disc is rotating with an electric motor operated arrangement. A shutter control relay operates the system shutter and automatically closes it when the preprogrammed film thickness is achieved.

Thin films of ZnO nanostructures were characterized for their microstructure by using SIEMENS D5000 x-ray diffractometer (XRD) equipped with Cu-K_α (λ = 1.544 Å) radiation source. The crystallographic information/hierarchical lattice structure were also obtained from selected area electron diffraction (SAED) pattern and high resolution image in JEOL 2010 high resolution transmission electron microscopy (HRTEM). The ZnO nanostructures were separated from as-grown Si samples dipped in ethanol by ultrasonically shaking for 30-45 minutes at 30 ºC. The HRTEM grid was prepared by

putting a droplet from the acquired ZnO solution containing ZnO nanostructures after ultrasonic shaking for 10 minutes. The thickness of ZnO films was evaluated by using Tencor P-10 surface profilometer. The surface morphology of as-grown nanostructures, their size distribution, elemental composition and distribution were investigated by using a JEOL JSM-6300F field-emission scanning electron microscopy (FESEM) equipped with energy dispersive x-ray spectroscopy (EDS) attachment. The synthesized ZnO thin films are depicted with distinct diversity as randomly oriented 1-dimensional (1-D) and multipod (tripod and tetrapod)-like nanostructures of varying diameters when revealed by the investigations. Raman spectroscopy of the ZnO nanostructures was performed by analyzing phonon frequencies in a backscattering geometry using a Renishaw MicroRaman spectrometer equipped with a 514.5 nm continuous wave Argon ion (Ar^+) laser and having spectral resolution of 1 cm^{-1}.

3. Results and discussions (Characterization of ZnO thin films)

3.2. Film thickness profile

Figure 1 provides the thickness profile acquired by surface profilometer for a typical ZnO thin film deposited for 0.04 nm/sec rate. The ZnO film is ~150 nm thick. The dips in the profile present the vertical spaces between the columnar nanostructures when scanned from the top of the film. The spaces are developed during onset of seed growth and may left unfilled during rapid phase evolution. The nanowires grow as 1-dimensional nanostructures on the Si surface for this typical deposition rate of 0.04 nm/sec. The film thickness is found to be ~150 nm. ZnO films are found to be almost same thickness, as revealed from all the film samples deposited for various deposition rates.

3.3. Microstructural analysis

Figure 2 provides XRD spectra, recorded in locked-couple and detector scan mode, of the ZnO thin films deposited on Si for different deposition rates. The spectra in figure 2a clearly show the growth of hexagonal ZnO with the emergence of (101) plane at 2θ = 36.28º and (201) plane at 2θ = 68.79º (database pattern 01-087-0713) along with the presence of (100), (101), (102) and (103) planes of Zn for 0.01 and 0.02 nm/sec deposition rates. Whereas, for 0.04 nm/sec rate, ZnO appears with (201) plane orientation only at 2θ =68.5º, as depicted by the prominent intense peak in the inset figure 2c with high resolution. Thus, ZnO films deposited at 0.04 nm/sec are more crystalline as compared to those deposited at 0.01 and 0.02 nm/sec. For 0.06 nm/sec rate, ZnO grows in multipod-like structures with no remarkable XRD peak. The inset of figure 2a more clearly resolves the peaks and shows the emergence of (311) peak at 2θ =69.6º corresponding to SiO_2 at the film-substrate interface, for this deposition rate. The interface oxide (SiO_2) layer, natively present, provides the base for the growth of ZnO nanostructures.

XRD spectra recorded in detector scan mode (figure 2b) provide (112) diffraction plane of hexagonal ZnO at 2θ = 67.62º having lattice parameters $a = b = 3.24$ Å and $c = 5.2$ Å (database pattern 03-065-3411), along with the presence of (-264) peak of triclinic zinc silicate Zn_2SiO_4 at 2θ = 67.62º with lattice parameters $a = 5.1$ Å, $b = 9.94$ Å and $c = 15.90$ Å (database pattern 00-019-1479, CAS number: 13597-65-4) for both deposition rates of 0.01 and 0.02 nm/sec. Zn_2SiO_4 is formed due to the availability of oxygen ion vacancy, which leads to the formation of unstable non-stoichiometric $Zn_{1+x}O$. This phase interacts with Si atoms of the substrate to form Zn_2SiO_4. For 0.04 nm/sec rate the diffraction peak (201) is not visible (as seen in figure 2a), possibly due to the structural

orientation of the atoms in the detector scan. XRD spectra show that there is little possibility of contamination during the nanowires growth, probably due to residual air in the evacuated chamber. Moreover, the calcination of zinc oxide in ambient air and subsequent pressing into pellet may also introduce some trace level of impurities. XRD spectra in both scan modes show no diffraction peak for 0.06 nm/sec deposition rate, possibly due to lesser time available for adatoms rearrangement into lattice for faster evaporation rates and also as substrates were not heated.

The crystallite size *D* and dislocation density δ calculated for the preferential orientation provide crystalline quality of ZnO films. The average crystallite size, *D*, calculated by the Scherrer formula is ~90 nm, which shows good crystallinity of ZnO thin films deposited for 0.04 nm/sec. The negligible shift in the diffraction peak positions from their corresponding stress free data shows that the ZnO films deposited for 0.04 nm/sec rate have almost no stresses. This suggests that the thermally evaporated deposits inhibit any stress evolution during deposition at a particular rate, when carried out at/near room temperature. For this typical deposition rate of 0.04 nm/sec, the dislocation density δ calculated by the formula [35]

$$\delta = 1 / D^2$$

is obtained as 1.23×10^{-4} $(nm)^{-2}$.

3.4. FESEM/EDS analysis

Figure 3(a–d) shows typical FESEM micrographs of the ZnO thin films deposited for deposition rates of 0.01, 0.02, 0.04 & 0.06 nm/sec. Micrographs at low magnification (inset figures 3a1, 3b1, 3c1 & 3d1) display a large area uniformity of the ZnO nanostructures deposition on Si. Same level of surface coverage uniformity has been

confirmed on Si substrates for complete lot of samples synthesized at each deposition rate. This reflects a better yield of high quality ZnO nanostructures production by thermal evaporation in catalyst free environment. Interestingly, the ZnO thin films show the nanostructures growth with distinct surface morphology for different deposition rates.

For deposition rates of 0.01 and 0.02 nm/sec, randomly oriented ZnO nanowires of ~ 60 – 70 nm diameters grow with almost identical morphology (figures 3a & 3b). A seeding layer comprised of ZnO grains is developed on Si by thermal evaporation of ZnO powder at preliminary growth stage. Nanowires subsequently nucleate at the apices of the ZnO grains. The nanowires can be identified as coagulated in some regions, owing to the growth-induced surface tension in the seeding layer. For 0.02 nm/sec rate, the coagulation factor of nanowires is little higher.

For 0.04 nm/sec deposition rate, 1-D vertically oriented ZnO nanowires grow covering the whole surface of the Si substrate uniformly (figure 3c). The nanowires have diameter of ~ 50 -60 nm, as is obvious from the top view FESEM scan. The diameter is confirmed on multiple positions of the film surface. The space between the nanowires makes them suitable to be bent for generating the piezoelectric potential [36]. It has been inferred that the orientation of the ZnO nanowires growth could be controlled if thin layer of ZnO with good vertical c-axis orientation was developed on the substrate before the subsequent growth by thermal evaporation [29].

For 0.06 nm/sec deposition rate, ZnO nanostructures grow uniquely as multipods (tripods and tetrapods) (figure 3d). The multipods have diameter in the range of 150-250 nm whereas arm length varies from 500-800 nm. A multipod may have a nanowire arm growth in 2-3 stages with a total length varying from 1 to 2 μm. The branched

nanostructures are uniquely projected from a single origin on the stem of a nanowire. The projected branches can grow as hexagonal- and cylindrical-shaped nanowires of ~90-100 nm diameters. This structural growth reflected by the presence of multiple growth phases of ZnO nanostructure, is probably stimulated by the special structure of nanoseeds for this deposition rate.

The elemental composition and distribution of ZnO nanowires were investigated by EDS. A typical EDS spectrum of ZnO film deposited for 0.02 nm/sec (figure 4a) confirms that ZnO thin film nanostructures are composed of Zn and O elements only, along with Si as balance. EDS profile of the films deposited for lower deposition rate have little level of O content deficiency. For 04 nm/sec rate (Figure 4b), Zn & O contents show good stoichiometry in the ZnO composition. While increasing film deposited rate to 0.06 nm/sec, the O content deficiency is enhanced. There may exist little amount of impurities in the ZnO nanowire that may fall below the detection limit of EDS. EDS maps (figures 4c & 4d) sowing Zn and O distribution in the ZnO films deposited for 0.02 nm/sec also exhibit their uniform spatial profile. The elemental maps were recorded at various positions on random samples and same level of elemental spatial uniformity was observed. This reveals the homogeneous surface coverage of the Si samples with ZnO nanostructures deposited by thermal evaporation.

3.5. HRTEM analysis

Figure 5a presents a TEM image of frequently observed randomly oriented ZnO nanowires grown for 0.01 nm/sec deposition rate. The inset figure 5b provides the TEM image of a typical nanosnake-like structure for this deposition rate. The nanowires have diameter of 60-70 nm that is quite consistent with the FESEM investigations. The

discontinuity of a particular texture (stacking fault zone) is obvious at the dark bands appearing on the nanowires, which is caused by the small impurity concentration at the lattice site. The magnified TEM image (figure 5c) obtained from the lateral view of a ZnO nanowire also exhibits the stacking fault zone in a particular texture during crystal growth. The kink regions contain stacking faults marked as 1 and 2 in TEM images (figures 5a and 5c).

The HRTEM image shown in figure 5d reveals the atomic structure of a typical kink region (marked as 1 in figure 5a) of ZnO nanowire. It shows c-axis dominant crystal growth with the lattice spacing of a = 2.6 Å. In the region of only ZnO shell, the HRTEM image 5d shows clear lattice structure orientation shown by arrows in squares. The boundary between the Zn core and the ZnO shell is fairly sharp. Mismatch between the Zn core and ZnO shell produces defects and stacking faults in the interfacial region (marked as 1, 2 and 3 in image 5d). Such stacking faults have been analyzed in detail and are reported elsewhere [37]. The hexagon at the center shows the origination of a nanoseed with lattice structure. The hexagonal closed packed (hcp) model fitting clearly reflects the wurtzite ZnO growth facet. The corresponding SAED pattern of the kink region of nanowire is shown in figure 5e. The SAED analysis as well as XRD data indicate polycrystalline nature of the randomly oriented ZnO nanowires deposited for 0.01 and 0.02 nm/sec rates. Figure 5f provides the magnified view of hcp lattice structure having lattice spacing d = 2.8 Å in [01$\bar{1}$0] and d= 3.2 Å in [2$\bar{1}$ $\bar{1}$0] plane.

Figure 6a shows a typical magnified TEM image of 1-D ZnO nanowire (broken part of ~ 450 nm length) grown for 0.04 nm/sec deposition rate. Due to an inherent strong attachment on Si surface, only few of such 1-D nanowires could be obtained during

ultrasonic shaking of ZnO solution. This typical nanowire appears to be needle-like with a stem diameter of ~60 nm that becomes sharp near the tip with reduced diameter of ~ 40 nm. ZnO nanowires have hexagonal cross-section with a diameter in the range of 50-60 nm. The nanowire peripheral surfaces are smooth and clean, indicating that if needed they should be able to form reliable metal-semiconductor junctions needed for the nanowire nanogenerators. Such 1-D ZnO nanowire arrays have been innovatively used for the energy harvesting by employing their piezoelectric and semiconducting properties [3, 13]. The HRTEM image shown in figure 6b reveals the atomic structure of 1-D ZnO nanowire. From the HRTEM, the continuous lattice fringes indicate that the straight part of 1-D ZnO nanowire is fairly crystalline in nature, having the epilayer growth along [0001] c-axis. The average spacing between adjacent lattice planes perpendicular to the wire axis is 5.2 Å, which is in agreement with the distance between two (002) crystal planes of wurtzite ZnO. The inset figure 6c shows a SAED pattern (its corresponding Fast Fourier transform (FFT) along the (001) zone axis). From the lattice fringes and its FFT profile, the 1-D nanowire could be indexed to be a wurtzite structure of ZnO.

Figure 6d shows a typical TEM image of ZnO multipod nanostructures deposited for 0.06 nm/sec. Tripods and tetrapods of ~150 nm diameters are clearly visible as nanowires junctions. The nanowires have diameter of 50-60 nm. The image shows some coagulated regions (marked as 1 and 2 in figure 6d). Coagulation of nanostructures is due to the maximization of areas of [2$\bar{1}$ $\bar{1}$0] and [01$\bar{1}$0] facets because of their lower energy. In order to further verify the crystallography, the corresponding HRTEM image of a typical ZnO tripod (marked T in figure 6d) is shown in figure 6e. The d-spacing between adjacent

lattice planes on average is 2.6 Å that is ascribed to (001) plane of ZnO, further confirming the wurtzite phase.

3.6. Raman spectroscopy analysis

Figure 7 provides micro-Raman spectra taken at room temperature in order to investigate fundamental optical modes of ZnO nanostructures obtained for deposition rates of 0.01, 0.02, 0.04 and 0.06 nm/sec. Raman spectra have confirmed the appearance of LO and TO modes of ZnO depending on deposition rate. ZnO nanowires deposited for 0.01 and 0.02 nm/sec rates (figures 7a & 7b) have almost identical Raman profiles. The peaks located at 390, 415, 439 and 564 cm^{-1} respectively correspond to the A1(TO), E1(TO), E2(high) and A1(LO) phonon modes of wurtzite ZnO [38, 39]. The peak at 313 cm^{-1} should be assigned to the second-order Raman scattering. This conforms well to that observed by Gao et al. [40] during investigations on ZnO nanorods. The peak at 439 cm^{-1} assigned to E2 mode involves mainly a Zn motion corresponding to the band characteristic of the wurtzite phase of ZnO.

The peak at 390 cm^{-1} assigned to A1(TO) mode indicates the presence of some degree of structural disorder in the ZnO lattice. It owes to the small level of stresses due to the local heating effects during the synthesis. A1(TO) mode, which is difficult to obtain due to the destructive interference between the Frohlich interaction and the deformation-potential contributions to the LO-phonon scattering [38], is weakly present in the Raman spectra for all the ZnO films. The appearance of A1(TO) and E2(high) Raman modes is also in conformity with the observation by Wu et al. [41] on the ZnO nanowires prepared via sol-gel template route. The band extending from ~ 500-590 cm^{-1} is de-convolved by Gauss peak fitting into two peaks centered at ~540 cm^{-1} and 564 cm^{-1}. The peak at 540

cm^{-1} is the contribution of the E1 (LO) mode of ZnO associated with oxygen deficiency whereas the peak at 564 cm^{-1} assigned to A1(LO) could be attributed to the Zn interstitials present in the films. The E1 mode splitting into TO and LO components is caused by the macroscopic electric fields. The envelope of bands above 1090 cm^{-1} can be attributed to overtones and/or combination bands [42], which appear in the spectra of films deposited for 0.01, 0.02 and 0.06 nm/sec rates (figures 7a, 7b & 7d).

3.7 Growth kinetics of ZnO nanostructures

Control over growth kinetics is vital in determining the nanostructures formation that is a complex and less understood area. ZnO can grow in a wide range of novel structures by tuning various process parameters during the thermal vaporization [43]. FESEM and TEM results show that ZnO nanostructures have distinct dissimilarities; changing from randomly oriented nanostructures to 1-D nanowires and multipods (tripods and tetrapods) with increasing deposition rate. The possible growth mechanism can be assumed to be the vapor-solid (VS) process as no metal catalyst is used. Zn evaporation as a violent breakout process undergoes oxidation to form ZnO*x* vapors expressed as

$$ZnO(s) \leftrightarrow ZnOx\ (g) \qquad (1)$$

$$ZnOx\ (g) \leftrightarrow Zn(g) + (1/2)\ O_2(g) \qquad (2)$$

Although a part of the ZnO*x* vapors decomposes into Zn vapor and O_2 they, together with the Zn vapors, are transported downstream and deposited on the Si substrate to nucleate at an early stage by condensation. ZnO crystal grows preferentially along (001) direction due to lowest surface energy of the (002) facet. Further evaporation, oxidization and nucleation cause homogeneous epitaxial growth of ZnO nanostructures [44]. With increasing deposition rate, the concentration of vaporized Zn species increases

influencing significantly the morphology of the ZnO products due to different deposited ratios [32], as supported by our EDS results also.

At lower deposition rates, the Zn and ZnO*x* vapors generation and the eventual ZnO crystallization are relatively slow. Figure 3e shows FESEM micrograph of typical nanowires deposited for 0.01nm/sec rate. The precursor growth proceeds and results in the formation of nanowires along with the further deposition of ZnO*x* vapors. The precursor growth to deposition ratio is >1. Eventually, growth proceeds in multiple stages connected by joints containing small dislocations. Dislocations observed in joints play an important role in the strain relaxation [45] in these regions and eventual multiple growth of ZnO in various facets. The random directionality represents small stresses in the nanowires. At each joint, the nanowire suffers bending (kinks) based on the level of stress. The possible lateral growth in transverse geometry of nanostructures i.e. [01$\bar{1}$0] and [2$\bar{1}$ $\bar{1}$0] planes causes coagulation during multiple growth stages.

A typical FESEM micrograph obtained at tilt angle of 45^{o} for ZnO film grown at 0.04 nm/sec rate is depicted in figure 3f. For a higher deposition rate of 0.04 nm/sec, there is increased Zn species (as verified by EDS). Thus, the precursor growth to incoming vapor deposition ratio is assumed to be unity. This would have favored the nucleation and successive growth in 1-D. Neither the precursor growth overcomes the deposition rate to evolve a stressed nanostructure nor would the growth mode be supersaturated. This change in growth kinetics leads to the fast growth of 1-D nanowires along [0001] direction. It has been suggested that there exists an asymmetry along the c-axis promoting this anisotropic growth owing to absence of center of inversion in a hexagonal structure. Notably, XRD results also show better crystallinity and negligibly stressed growth texture

of ZnO nanostructures deposited at rate of 0.04 nm/sec. Thus, the axial growth exceeds the lateral growth rate and dictates 1-D shape for low supersaturation from crystallographic point of view [46, 47].

On further increasing the deposition rate to 0.06 nm/sec, the precursor growth to deposition ratio becomes <1 and the growth is supersaturated because of ZnO*x* vapors abundance. The supersaturation causes branching of nanowires at each node or joint that results in the multipods (tripods and tetrapods). Thermodynamically, the ±[2$\bar{1}$ $\bar{1}$0] planes are relatively low energy surfaces forming the top/bottom surface of the branches. The nuclei of the new ZnO branches are formed only on the (0001) Zn-polar surface. The nanoseed structure, possessing a particular facet, is assumed to be the key factor in promoting such polytypic growth process owing to following reasons; (i) The branches originate from a specific region having a peculiar structure in the stem of nanowire, (ii) The projected branches protrude outward in a particular crystallographic plane in the stem. A typical multipod imaged at much higher magnification of ×250,000 (figure 3f1) appears to be comprised of numerous growth facets (seeds). The likelihood of the growth for a particular facet is dictated by the crystal growth kinetics involving relative surface activities under those conditions.

The [0001] direction becomes the fastest growth direction for branching nanorods. The communal growth of three directions can form short and cuboid branches (figure 3d), rather than to form ordinary thin and rod-like branches. We can hypothesize that the formation of multipod nanostructures could be via a multiphase crystal growth process induced by a specific structure in the nanoseed. Zn^{+2} is shifted from the center of octahedron with O^{-} at vertices, and the crystal does not possess inversion symmetry,

showing a large spontaneous polarization along [0001] direction. The electrostatic interaction energy and distinct chemical activities of the polar surfaces result in the formation of a wide range of structures. Zn^{+2} (0001) surface is chemically active and O^{-} (0001) surface is relatively inert, resulting in growth of long fingers along [0001] direction. Zn-terminated surface has tiny Zn clusters, which lead to self-catalyzed growth in the absence of foreign catalyst [48]. Research findings suggest that the deposition rate is one of the effective parameters controlling morphology of ZnO nanostructures when evaporation is carried out in background air at low pressure. Nevertheless, the growth mechanism for ZnO nanowire 1-D arrays and multipods still necessitates further extensive research work.

4. Conclusions

ZnO thin films comprised of randomly oriented, 1-D and multipods (tripods and tetrapods)-like hetrostructures have been grown on Si substrates by thermal evaporation using a catalyst-free 99.99% ZnO powder. The ZnO films of 150 nm thickness were selectively grown for various deposition rates (0.01, 0.02, 0.04 and 0.06 nm/sec). XRD analysis confirmed the polycrystalline nature of wurtzite ZnO nanowires with the lattice constant $a = b = 3.24$ Å and $c = 5.2$ Å. FESEM and HRTEM revealed a strong influence of deposition rate on the morphology of nanowires. The deposition rates of 0.01 and 0.02 nm/sec dictated randomly oriented ZnO nanowires of about 60-70 nm diameter and 2-3 stage arm growth with total length of ~2μm. For a typical deposition rate of 0.04 nm/sec, aligned (1-D) ZnO wires were grown with high aspect ratio and hexagonal cross-section of ~50-60 nm diameter. For 0.06 nm/sec deposition rate, multipod (tripod and tetrapod)-like nanostructures are grown with 2-3 stage arm growth of ~1-2 μm length. Micro

Raman spectra of the films confirmed appearance of LO and TO modes of ZnO dependent on the deposition rate. The envelope of combination bands appears in the spectrum of films deposited for 0.01, 0.02 and 0.06 nm/sec rates. The distinct nanostructure formation is via a multiphase growth process induced by a specific structure in the ZnO nanoseed.

Acknowledgements

The authors are grateful to the National Institute of Education/ Nanyang Technological University, Singapore, for AcRF grant RI 7/08 RSR to conduct this research work.

References

[1] Z.L. Wang, J. Phys: Condens. Matter. **16,** R829 (2004).

[2] R. Yang, Y. Qin, L. Dai, Z.L. Wang, Nature Nanotechnol. Lett. **4,** 34 (2009).

[3] Z.L. Wang, Adv. Funct. Mater. **18,** 3553 (2008).

[4] Z.W. Pan, Z.R. Dai, Z.L. Wang, Science **291,** 1947 (2001).

[5] X.Y. Kong, Z.L. Wang, Appl. Phys. Lett. **84,** 975+cover (2004).

[6] X.Y. Kong, Y. Ding, R. Yang, Z.L. Wang, Science **303,** 1384 (2004).

[7] P.X. Gao, Y. Ding, W. Mai, W.L. Hughes, C.S Lao, Z.L. Wang, Science **309,** 1700 (2005).

[8] F. Liu, P.J. Cao, H.R. Zhang, J.Q. Li, H.J. Gao, Nanotechnology **15,** 949 (2004).

[9] X.D. Wang, C.J. Summers, Z.L. Wang, Nano Lett. **4,** 423 (2004).

[10] Y. Wu, X.H. Zhang, F. Xu, L.S. Zhang, J. Kang, Nanotechnology **20(32),** 325709 (2009).

[11] Y. Kozuka, A. Tsukazaki, M. Kawasaki, Appl. Phys. Rev. **1,** 011303 (2014).

[12] J. He, X. Zheng, X. Hong, W. Wang, Y. Cao, T. Chen, L. Kong, Y. Wu, Z. Wu, J. Kang, Mater. Lett. **216,** 182 (2018).

[13] J. Zhou, Y. Gu, P. Fei, W. Mai, Y. Gao, R. Yang, G. Bao, Z.L. Wang, Nano Lett. **8(9),** 3035 (2008).

[14] J. Zhou, N. Xu, Z.L. Wang, Adv. Mater. **18,** 2432 (2006).

[15] V.P. Singh, K. Sandeep, H.S. Kushwaha, S. Powar, R. Vaish, Constr. Build. Mater. **158,** 285 (2018).

[16] X. Wang, J. Song, J. Liu, Z.L. Wang, Science **316,** 102 (2007).

[17] J. Liu, P. Fei, J. Zhou, R. Tummala, Z.L. Wang, Appl. Phys. Lett. **92,** 173105 (2008).

[18] Y. Qin, X. Wang, Z.L. Wang, Nature Lett. **451,** 809 (2008).

[19] Z.L. Wang, J.H. Song, Science **312,** 242 (2006).

[20] Y. Li, F. Qian, J. Xiang, C.M. Lieber, Mater. Today **9,** 18 (2006).

[21] G.F. Zheng, F. Patolsky, Y. Cui, W.U. Wang, C.M. Lieber, Nature Biotechnol. **23,** 1294 (2005).

[22] Z. Zhang, H. Yuan, Y. Gao, J. Wang, D. Liu, J. Shen, L. Liu, W. Zhou, S. Xie, X. Wang, X. Zhu, Y. Zhao, L. Sun, Appl. Phys. Lett. **90,** 153116 (2007).

[23] A.B. Djurisic, W.M. Kwok, Y.H. Leung, W.K. Chan, D.L. Phillips, M.S. Lin, S. Gwo, Nanotechnology **17(1),** 244 (2006).

[24] M.C. Newton, P.A. Warburton, Mater. Today **10,** 50 (2007).

[25] M. Erfan, L.M. Gnambodoe-Capochichi, F. Marty, Y.M. Sabry, T. Bourouina, Y. Leprince-Wang, Nanoscale **12,** 1397 (2020).

[26] Z.L. Wang, Mater. Today **10(5),** 20 (2007).

[27] Z.L. Wang, MRS Bulletin **32,** 109 (2007).

[28] P.C. Chang, Z.Y. Fan, D.W. Wang, W.Y. Tseng, W.A. Chiou, J. Hong, J.G. Lu, Chem. Mater. **16,** 5133 (2004).

[29] W. Lee, M. Jeong, J. Myoung, Acta Materialia **52,** 3949 (2004).

[30] R.B.M. Cross, M.M. De Souza, E.M.S. Narayanan, Nanotechnology **16,** 2188 (2005).

[31] B.D. Yao, Y.F. Chan, N. Wang, Appl. Phys. Lett. **81,** 757 (2002).

[32] S. Xu, Y. Wei, M. Kirkham, J. Liu, W. Mai, D. Davidovic, R.L. Snyder, Z.L. Wang, J. Am. Chem. Soc. **130(45),** 14958 (2008).

[33] E. Mosquera, M.J. Morel, J.E. Diosa, Appl. Phys. A **125(9),** 613 (2019).

[34] D. Yuvaraj, M. Sathyanarayanan, K.N. Rao, Appl. Nanosci. **4,** 801 (2014).

[35] V. Bilgin, S. Kose, F. Atay, I. Akyuz, Mater. Chem. Phys. **94**, 103 (2005).

[36] Y.F. Gao, Z.L. Wang, Nano lett. **7(8),** 2499 (2007).

[37] Y. Ding, X.Y. Kong, Z.L. Wang, J. Appl. Phys. **95,** 306 (2004).

[38] U. Ozgur, Y.I. Alivov, C. Liu, A. Teke, M.A. Reshchikov, S. Dogan, V. Avrutin, S.J. Cho, H. Morkoc, J. Appl. Phys. **98,** 041301 (2005).

[39] J. Serrano, F.J. Manjon, A.H. Romero, A. Ivanov, R. Lauck, M. Cardona, M. Krisch, Phys. Status Solidi b **244,** 1478 (2007).

[40] H. Gao, F. Yan, J. Li, Y. Zeng, J. Wang, J. Phys. D: Appl. Phys. **40,** 3654 (2007).

[41] G.S. Wu, T. Xie, X.Y. Yuan, Y. Li, L. Yang, Y.H. Xiao, L.D. Zhang, Solid State Commun. **134(7),** 485 (2005).

[42] A.P. de Moura, R.C. Lima, M.L. Moreira, D.P. Volanti, J.W.M. Espinosa, M.O. Orlandi, P.S. Pizani, J.A. Varela, E. Longo, Solid State Ionics **181(15-16),** 775 (2010).

[43] Z.R. Dai, Z.W. Pan, Z.L. Wang, Adv. Funct. Mater. **13,** 9 (2003).

[44] G.Z. Shen, Y.S. Bando, B.D. Liu, D. Golberg, C.J. Lee, Adv. Funct. Mater. **16,** 410 (2006).

[45] C. Huang, M. Wang, Y. Cao, Q. Liu, Z. Huang, Y. Liu, W. Guo, Q. Huang, J. Phys. D: Appl. Phys. **42,** 165306 (2009).

[46] G.J. Jiang, H.R. Zhuang, J. Zhang, M.L. Ruan, W.L. Li, F.Y. Wu, B.L. Zhang, J. Mater. Sci. **35,** 63 (2000).

[47] W. Seo, K. Koumoto, J. Am. Ceram. Soc. **79,** 1777 (1996).

[48] Z.L. Wang, X.Y. Kong, J.M. Zuo, Phys. Rev. Lett. **91,** 185502 + cover (2003).

Figure captions

Figure 1: Thickness profile, provided by surface profilometer, of a typical as-grown ZnO film on Si obtained for 0.04 nm/sec deposition rate.

Figure 2: XRD spectra, recorded in (a) locked couple scan mode and (b) detector scan mode, of the ZnO thin films deposited on Si for different deposition rates 0.01, 0.02, 0.04 and 0.06 nm/sec.

Figure 3: FESEM micrographs of the ZnO thin films deposited for deposition rates of (a) 0.01, (b) 0.02 (c) 0.04 and (d) 0.06 nm/sec. FESEM micrographs at low magnification (inset figures a1 at ×5000, b1 at ×7500, c1 at ×2500 & a4 at ×20000) exhibit a large area uniformity of the ZnO hetrostructures growth on Si for respective deposition rate. Typical FESEM micrographs (at high magnification) of ZnO films deposited for different deposition rates (e) 0.01 nm/sec (Nanowires), (f) 0.04 nm/sec, scanned at tilt angle: 45^{o} (1-D nanostructures) and (f1) 0.06 nm/sec (multipod). The multiple growth facets and 3 branches are clearly seen as c-axis orientation originating from the nanoseed.

Figure 4: Typical EDS spectra for the ZnO films deposited for (a) 0.02 nm/sec, (b) 0.04 nm/sec and typical EDS maps (c) Zn and (d) O distribution in ZnO thin film grown for deposition rate of 0.02 nm/sec.

Figure 5: TEM image of (a) randomly oriented nanowires grown for 0.02 nm/sec, (b) a typical nanosnake-like structure, (c) a typical arm/branch of nanowire showing multiple growth stages with kinks, (d) HRTEM image of a kink region marked in (a), (e) the corresponding selected area electron diffraction (SAED) pattern; The broad intensity distribution in SAED pattern near the centre indicates the crystallite sizes of few nanometers, and (f) magnified view of HRTEM image (d) showing the c-axis growth facet of hcp lattice structure of wurtzite ZnO nanoseed.

Figure 6: (a) TEM image, (b) corresponding HRTEM image and (c) selected area electron diffraction (SAED) pattern of 1-D ZnO nanowires grown for 0.04 nm/sec, (d) TEM image and (e) HRTEM image of the ZnO multipods (tetrapods/tripods) grown for 0.06 nm/sec.

Figure 7: Raman spectra of ZnO thin films grown for different deposition rates; (a) 0.01 nm/sec, (b) 0.02 nm/sec, (c) 0.04 nm/sec and (d) 0.06 nm/sec, taken under

backscattering geometry using the 514.5 nm of Ar^{+} laser as an excitation source (Lorentz fit of the experimental data). The band extending from 400-590 cm^{-1} has been de-convolved).

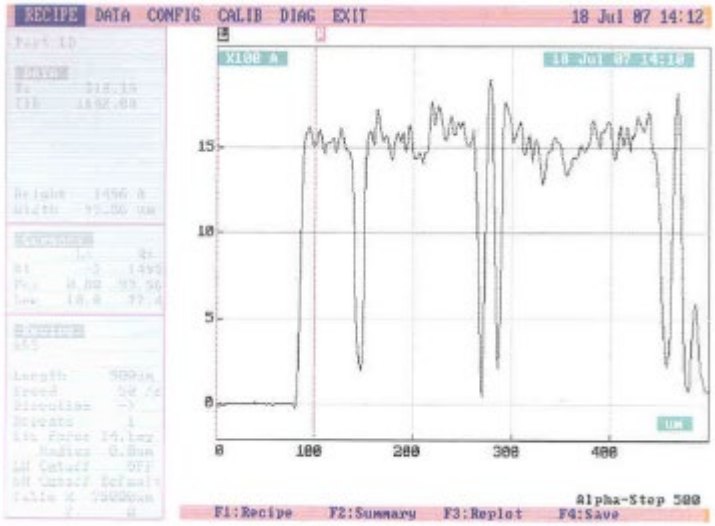
RECIPE DATA CONFIG CALIB DIAG EXIT
18 Jul 07 14:12
X100 A
18 Jul 07 14:18
15
10
5
0
0
100
200
300
400
um
Alpha-Step 500
F1:Recipe F2:Summary F3:Replot F4:Save
Thickness of ZnO Film: 15 × 100 Å = 150 nm

Figure 1

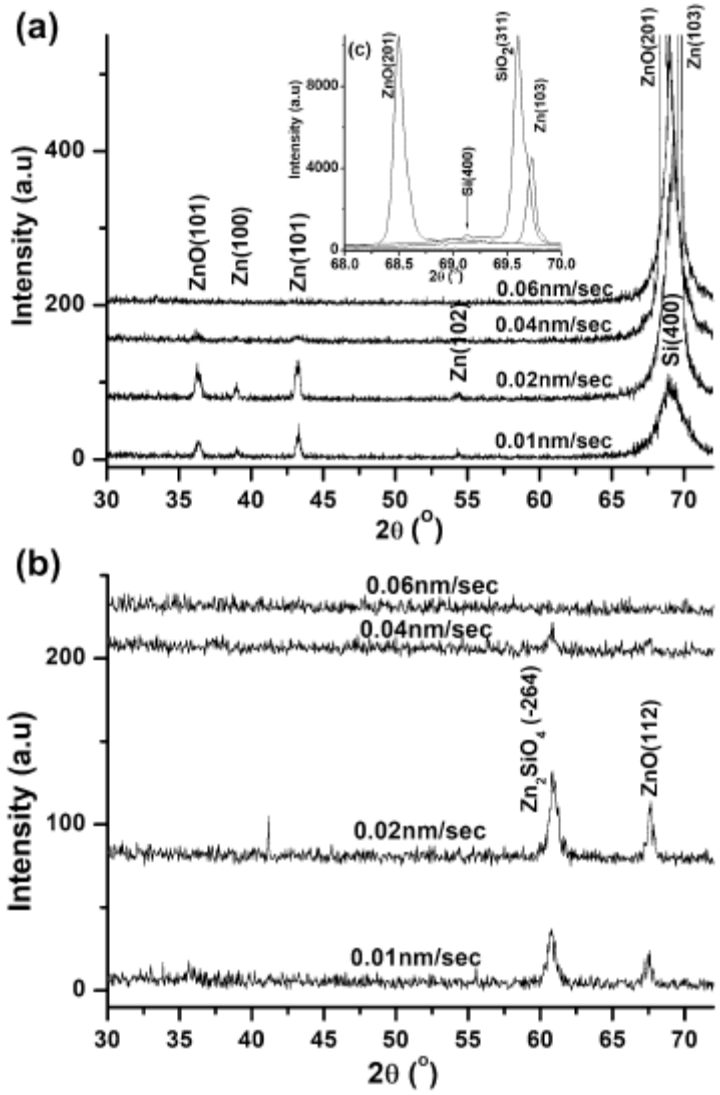
(a)
Intensity (a.u)
2θ (°)
ZnO(101)
Zn(100)
Zn(101)
Zn(102)
ZnO(201)
Zn(103)
Si(400)
0.06nm/sec
0.04nm/sec
0.02nm/sec
0.01nm/sec
(c)
Intensity (a.u)
ZnO(201)
Si(400)
SiO2(311)
Zn(103)
(b)
Intensity (a.u)
2θ (°)
0.06nm/sec
0.04nm/sec
Zn2SiO4 (-264)
ZnO(112)
0.02nm/sec
0.01nm/sec

Figure 2

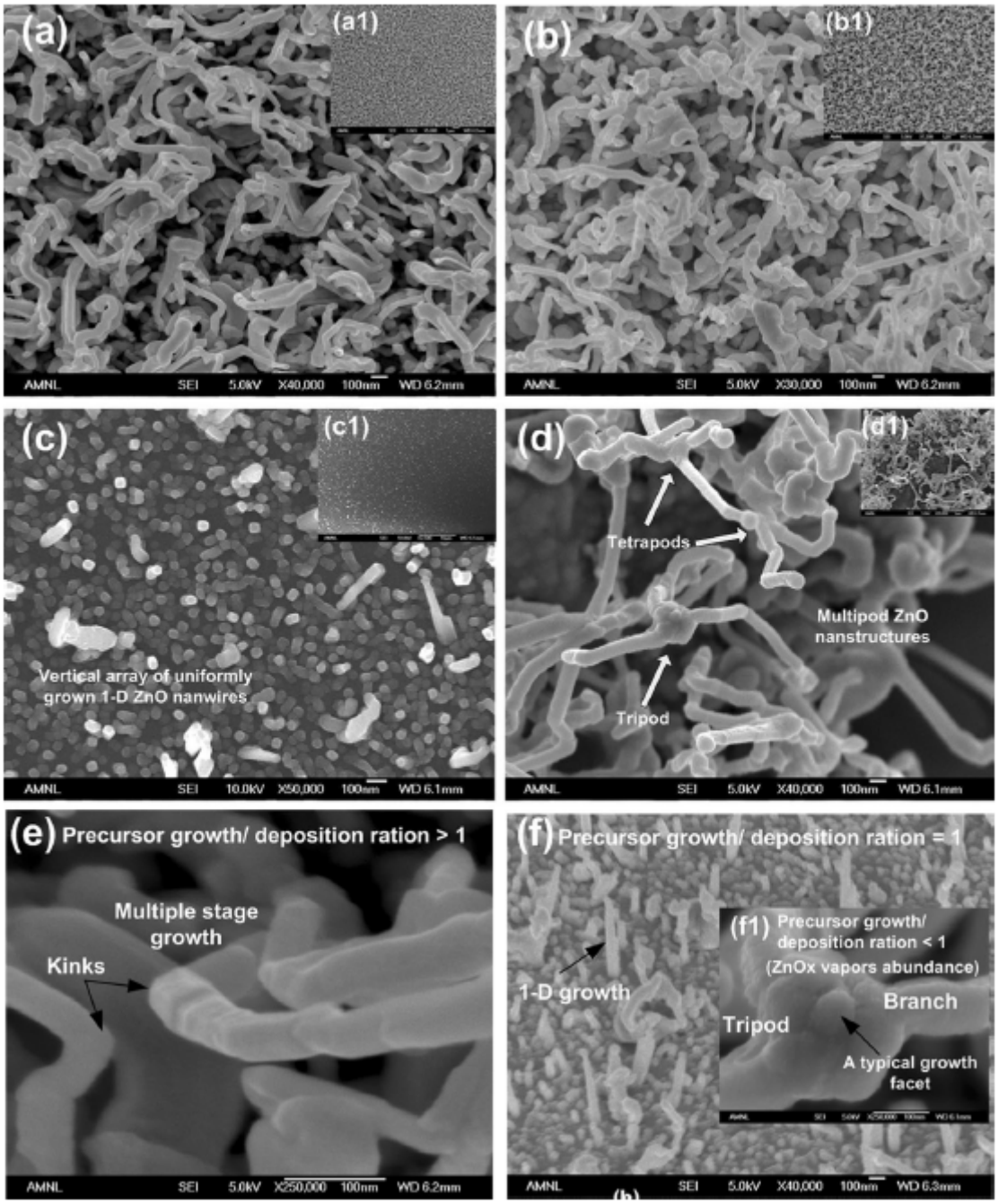
(a)
(a1)
AMNL SEI 5.0kV X40,000 100nm WD 6.2mm
(b)
(b1)
AMNL SEI 5.0kV X30,000 100nm WD 6.2mm
(c)
(c1)
Vertical array of uniformly grown 1-D ZnO nanwires
AMNL SEI 10.0kV X50,000 100nm WD 6.1mm
(d)
(d1)
Tetrapods
Multipod ZnO nanstructures
Tripod
AMNL SEI 5.0kV X40,000 100nm WD 6.1mm
(e) Precursor growth/ deposition ration > 1
Multiple stage growth
Kinks
AMNL SEI 5.0kV X250,000 100nm WD 6.2mm
(f) Precursor growth/ deposition ration = 1
(f1) Precursor growth/ deposition ration < 1
(ZnOx vapors abundance)
1-D growth
Branch
Tripod
A typical growth facet
AMNL SEI 5.0kV X40,000 100nm WD 6.3mm

Figure 3

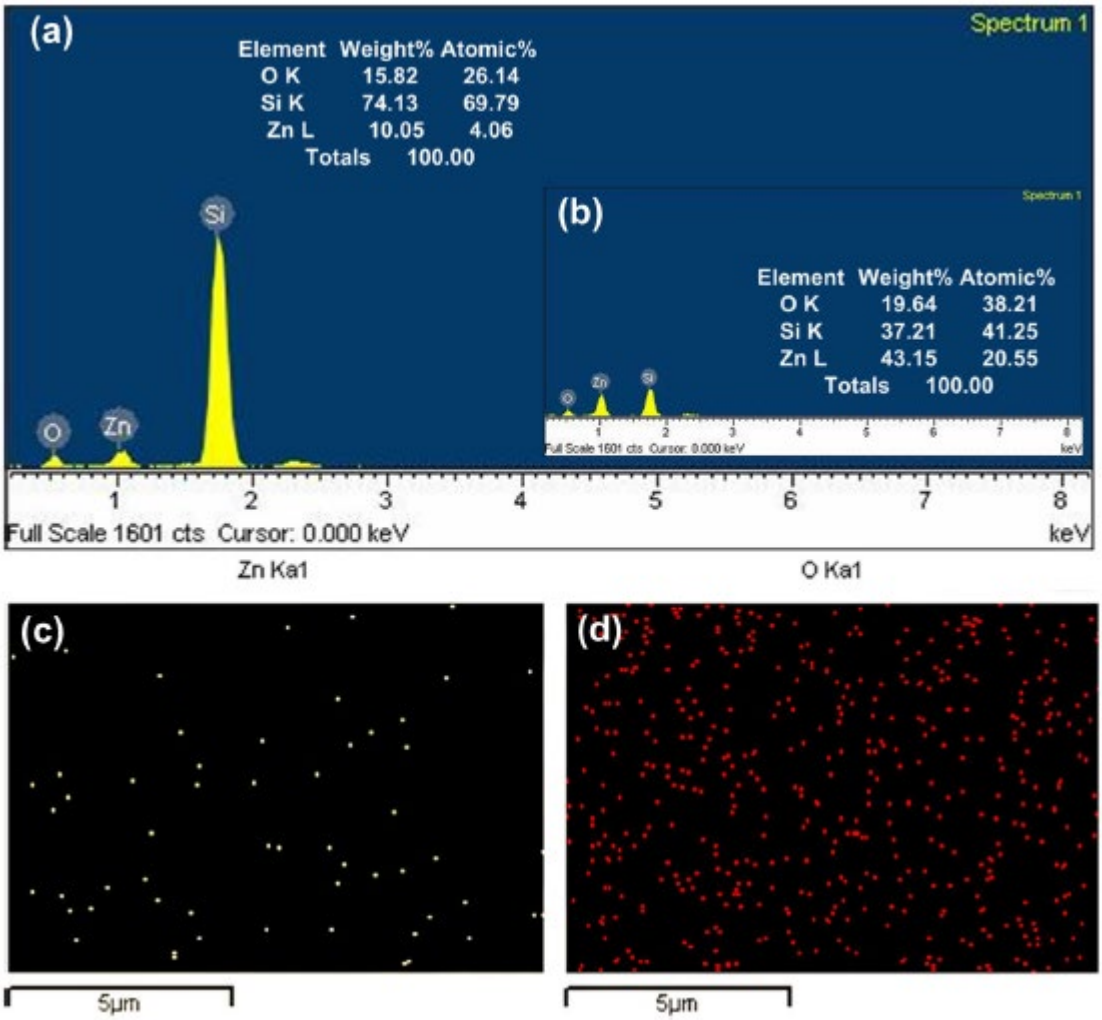
(a)
Spectrum 1
Element Weight% Atomic%
O K 15.82 26.14
Si K 74.13 69.79
Zn L 10.05 4.06
Totals 100.00
Si
O
Zn
(b)
Element Weight% Atomic%
O K 19.64 38.21
Si K 37.21 41.25
Zn L 43.15 20.55
Totals 100.00
1 2 3 4 5 6 7 8
Full Scale 1601 cts Cursor: 0.000 keV
keV
Zn Ka1
O Ka1
(c)
(d)
5µm
5µm

Figure 4

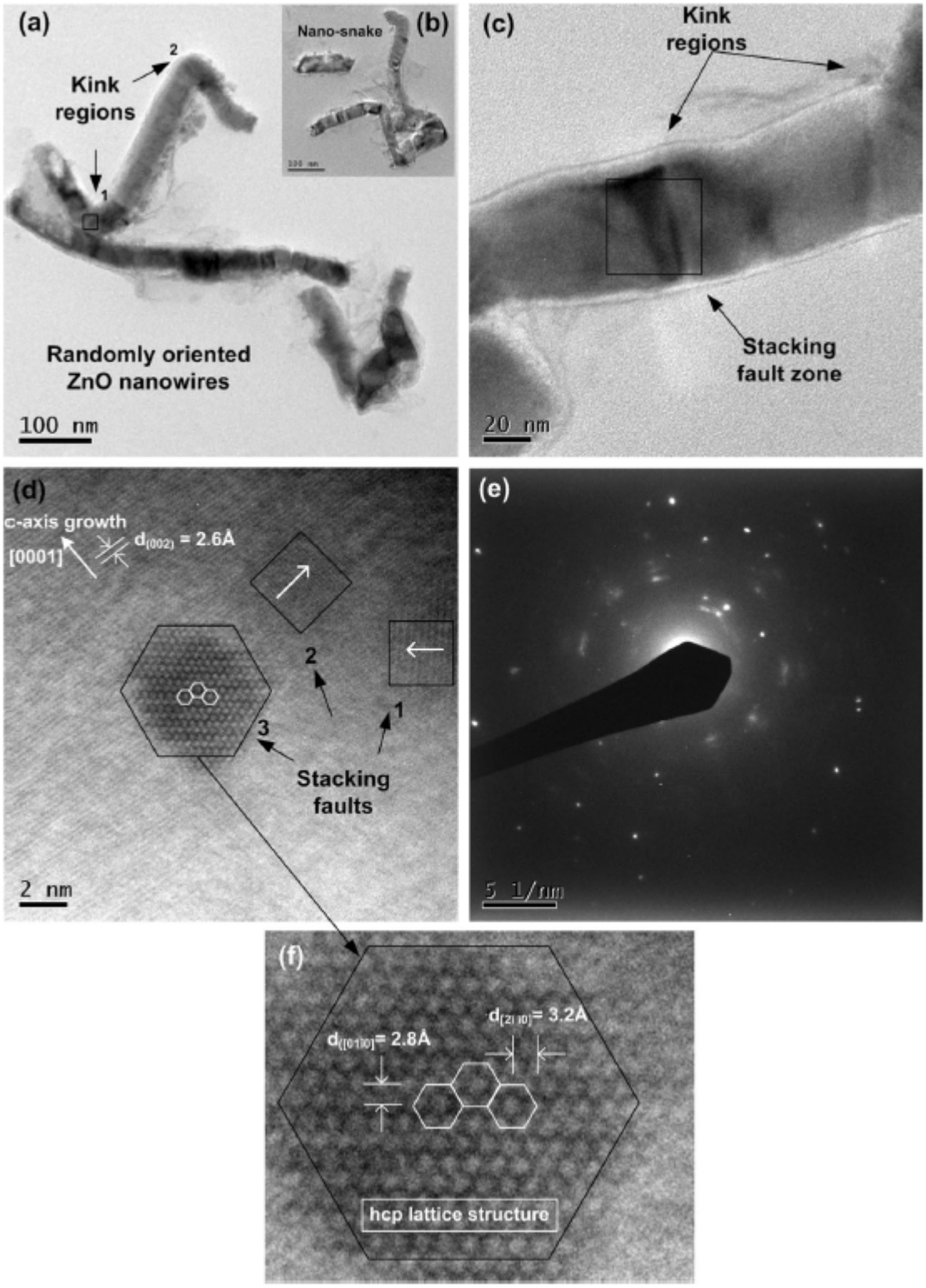
(a)
Kink regions
2
1
Randomly oriented ZnO nanowires
100 nm
(b)
Nano-snake
(c)
Kink regions
Stacking fault zone
20 nm
(d)
c-axis growth
[0001]
$d_{(002)}$ = 2.6Å
2
1
3
Stacking faults
2 nm
(e)
5 1/nm
(f)
$d_{[2\bar{1}\bar{1}0]}$= 3.2Å
$d_{[01\bar{1}0]}$= 2.8Å
hcp lattice structure

Figure 5

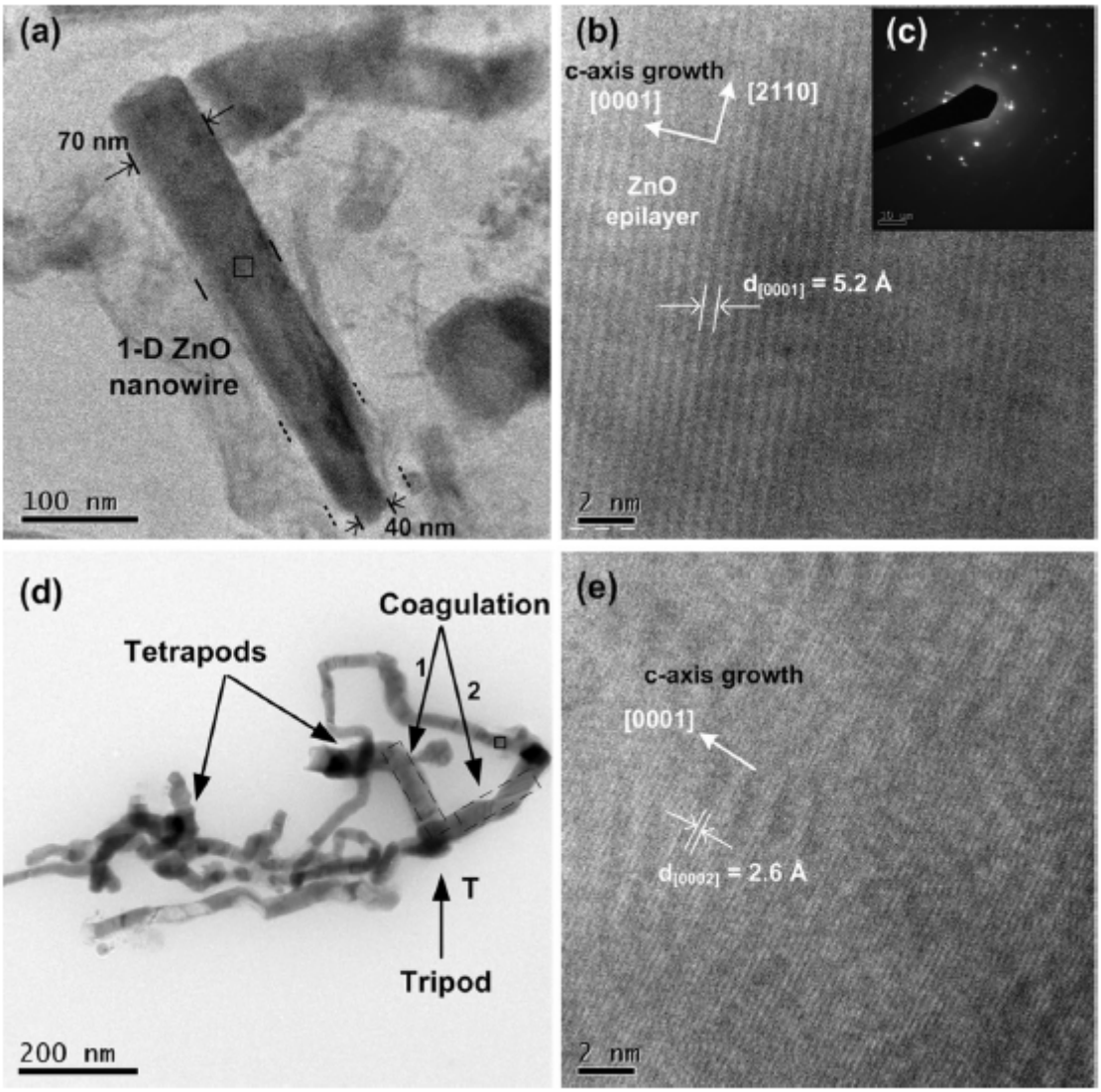
(a)
70 nm
1-D ZnO
nanowire
100 nm
40 nm
(b)
c-axis growth
[0001]
[2110]
ZnO
epilayer
d[0001] = 5.2 Å
2 nm
(c)
(d)
Coagulation
Tetrapods
1
2
T
Tripod
200 nm
(e)
c-axis growth
[0001]
d[0002] = 2.6 Å
2 nm

Figure 6

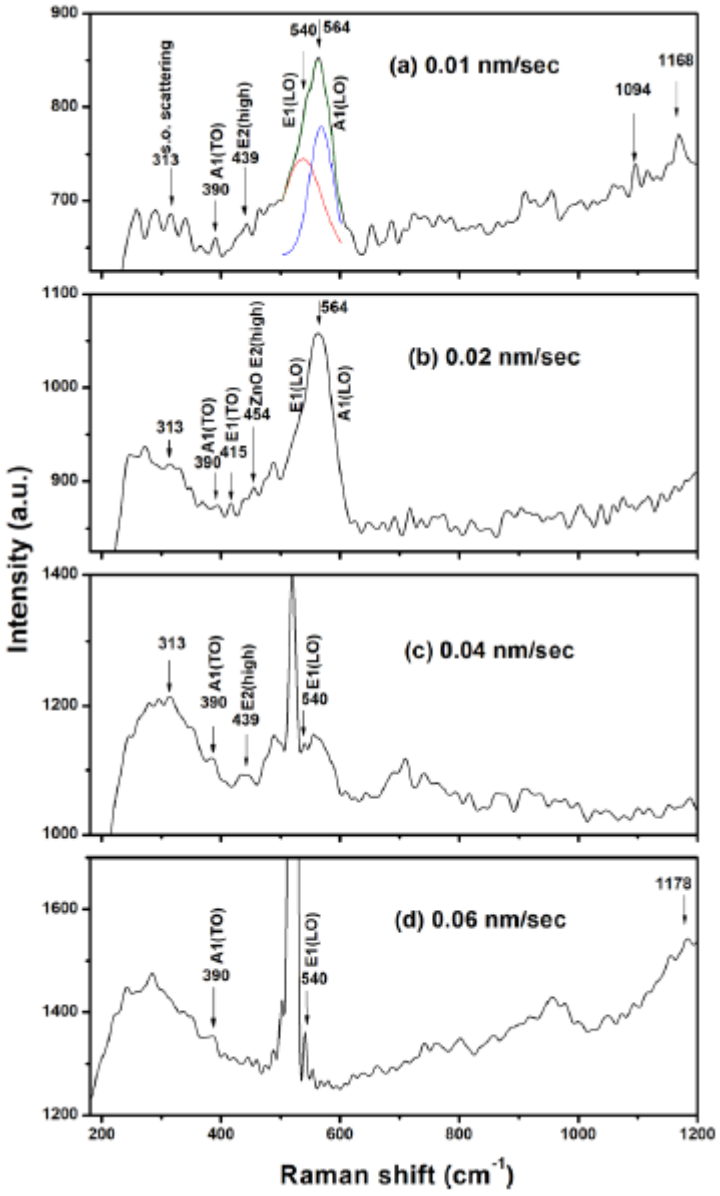
(a) 0.01 nm/sec
s.o. scattering
313
A1(TO)
390
E2(high)
439
E1(LO)
540
564
A1(LO)
1094
1168
(b) 0.02 nm/sec
313
A1(TO)
390
E1(TO)
415
ZnO E2(high)
454
E1(LO)
564
A1(LO)
(c) 0.04 nm/sec
313
A1(TO)
390
E2(high)
439
E1(LO)
540
(d) 0.06 nm/sec
A1(TO)
390
E1(LO)
540
1178
Intensity (a.u.)
Raman shift (cm-1)

Figure 7